

Spatially and Temporally Weighted Regression: A Novel Method to Produce Continuous Cloud-Free Landsat Imagery

Bin Chen, *Student Member, IEEE*, Bo Huang, *Associate Member, IEEE*, Lifan Chen, and Bing Xu

Abstract—Due to serious cloud contamination in optical satellite images, it is hard to acquire continuous cloud-free satellite observations, which limits the potential utilization of the available images and further data extraction and analysis. Thus, information reconstruction in cloud-contaminated images and the reprocessing of continuous cloud-free images are urgently needed for global change science. Many previous studies use one cloud-free reference image or multitemporal reference images to restore a target cloud-contaminated image; however, this paper is different and has developed a novel spatially and temporally weighted regression (STWR) model for cloud removal to produce continuous cloud-free Landsat images. The proposed method makes full utilization of cloud-free information from input Landsat scenes and employs a STWR model to optimally integrate complementary information from invariant similar pixels. Moreover, a prior modification term is added to minimize the biases derived from the spatially-weighted-regression-based prediction for each reference image. The results of the experimental tests with both simulated and actual Landsat series data show the proposed STWR can yield visually and quantitatively plausible recovery results. Compared with other cloud removal methods, our method produces lower biases and more robust efficacy. This approach provides a complete framework for continuous cloud removal and has the potential to be used for other optical images and to be applied to the reprocessing of cloud-free remote sensing productions.

Index Terms—Cloud removal, continuous cloud-free Landsat images, invariant similar pixels, spatially and temporally weighted regression (STWR).

I. INTRODUCTION

THE U.S. Geological Survey (USGS) Landsat program provides the longest temporal record of satellite-borne surface observations [1]. It has collected a history of how the Earth's land cover and land ecosystems have changed over the last 40 years, confronting increasing human population, natural resource demands, and climate change [2], [3]. With a change in data policy in 2008, the USGS released its Landsat archive to the public for free [4]. Due to the relatively high spatial resolution, Landsat data are experiencing more widespread use by an ever increasing range of end users in a variety of disciplines [2], which has greatly improved our understanding of the Earth's dynamics.

However, the primary limitation to the utility of optical remote sensing sensors such as the Landsat series is their sensitivity to weather conditions during data acquisition [5], [6]. It has been reported that Landsat ETM+ scenes are 35% cloud contaminated globally [7]. Thus, Landsat's 16-day revisiting cycle can be significantly lengthened due to frequent and uneven cloud contamination; moreover, complex topographic effects and equipment failure can further reduce the availability of images suitable for public usage and scientific analysis [8], [9]. For these reasons, the question of how to reconstruct continuous high-quality images without cloud contamination is an open topic for further research.

Several pioneering studies have attempted to address the issue of cloud removal. Based on the classification scheme proposed by Lin *et al.* [5], [10], here, we categorize existing methods into four major classes: self-complementation-based, multispectral-complementation-based, multitemporal-complementation-based, and auxiliary-sensor-complementation-based approaches. In the self-complementation-based approaches, without the incorporation of multispectral or multitemporal information, the cloud-contaminated regions are recovered by propagating the geometrical structure from the remaining cloud-free parts in the image. Spatial interpolation and image inpainting techniques are widely used in recovering small cloud gaps, and they can produce a visually plausible result, which is suitable for cloud-free visualization [10]. However, these types of methods could yield considerable biases when tackling

Manuscript received March 17, 2016; revised May 16, 2016; accepted June 8, 2016. This work was supported in part by the Ministry of Science and Technology of China through the National Research Program under Grant 2012AA12A407, Grant 2012CB955501, and Grant 2013AA122003; by the Hong Kong Research Grants Council through the General Research Fund under Grant 444612; and by the National Natural Science Foundation of China under Grant 41271099 and Grant 41371417.

B. Chen is with the State Key Laboratory of Remote Sensing Science, College of Global Change and Earth System Science, Beijing Normal University, Beijing 100875, China (e-mail: chenbin@mail.bnu.edu.cn).

B. Huang is with the Department of Geography and Resource Management, The Chinese University of Hong Kong, Shatin, Hong Kong (e-mail: bohuang@cuhk.edu.hk).

L. Chen is with the State Key Laboratory of Remote Sensing Science, College of Global Change and Earth System Science, Beijing Normal University, Beijing 100875, China, and also with the National Meteorological Information Center, China Meteorological Administration, Beijing 100081, China (e-mail: lifanchen@mail.bnu.edu.cn).

B. Xu is with the State Key Laboratory of Remote Sensing Science, College of Global Change and Earth System Science, Beijing Normal University, Beijing 100875, China; with the Ministry of Education Key Laboratory for Earth System Modeling, Center for Earth System Science, Tsinghua University, Beijing 100084, China; and also with the Department of Geography, University of Utah, Salt Lake City, UT 84112 USA (e-mail: bingxu@tsinghua.edu.cn).

Color versions of one or more of the figures in this paper are available online at <http://ieeexplore.ieee.org>.

Digital Object Identifier 10.1109/TGRS.2016.2580576

large-scale clouds or heterogeneous landscapes. In the multispectral-complementation-based approaches, the cloud-contaminated bands are recovered by modeling the relationship between cloud-contaminated bands and auxiliary clear bands. For example, Rakwatin *et al.* [11] reconstructed the missing data of Aqua Moderate Resolution Imaging Spectroradiometer (MODIS) band 6 using histogram matching and least-squares fitting functions derived from the relation between MODIS bands 6 and 7. Zhang *et al.* [12] proposed a haze optimized transformation method to radiometrically correct and compensate visible bands of Landsat images contaminated by thin clouds and haze. Ji [13] utilized the near infrared (NIR) band to estimate the spatial distribution of haze intensity in each visible bands through a linear regression model established over deep water. Due to the spectral dependence and comparability, this category of approaches yields a visually plausible result for thin clouds or haze contamination. However, it is incapable of removing thick clouds and restoring missing cloud-contaminated regions quantitatively.

Recently, some studies have attempted to remove clouds by fusing auxiliary information from different sensors, which is termed as an auxiliary-sensor-complementation-based approach. For example, Roy *et al.* [6] proposed predicting the missing data of Landsat images by incorporating the corresponding MODIS image. Hoan and Tateishi [14] developed a method to remove clouds in ALOS-AVNIR2 optical images with the aid of microwave images from ALOS-PALSAR data. Huang *et al.* [15] applied sparse representation and dictionary learning techniques to restore cloud-contaminated optical images by integrating SAR imagery. However, fusing information from other sensors is constrained by intrinsic differences in spatial resolution, spectral comparability, and temporal coherence. Moreover, performing cloud removal in this way requires more preprocessing steps and computation costs.

Compared with the three former categories of approaches, the multitemporal-complementation-based approaches seem to be more effective and achieve a better ability to cope with large and thick clouds. With a regular revisiting cycle, satellite use can provide multitemporal acquisitions of remote sensing images in the same region. The cloud-contaminated parts of these images cannot completely overlap all the time, which provides the cloud-free multitemporal reference to restore missing areas in the target image. Melgani [16], and Benabdelkader and Melgani [17] investigated the spacetemporal relations from the acquired multitemporal images to reconstruct cloud-contaminated areas. Li *et al.* [18] developed a technique to mosaic optimal cloud-free pixels from multitemporal images to generate cloud-free images. Similarly, Lin *et al.* [10] proposed a reconstruction of cloud-contaminated portions by cloning cloud-free information from multitemporal images. Zhu *et al.* [19] developed a modified neighborhood similar pixel interpolator (MNSPI) for thick cloud removal. Cheng *et al.* [20] proposed to remove clouds by similar pixel replacement guided by a cloud-free multitemporal image through a spatiotemporal Markov random field model (STMRF). In a similar fashion to the gap filling procedure, the local linear histogram matching (LLHM) method can also be employed to restore missing

values through a linear matching model between local cloud-free pixels in the target and reference images.

Nevertheless, most of existing multitemporal-complementation-based approaches require a cloud-free auxiliary image as a reference to mosaic cloud-free patches or locate similar pixels, which will be largely constrained by the availability of cloud-free observations. For example, Leckie [21] found that the probability of acquiring a cloud-free Landsat scene (cloud cover < 10%) can be as low as 10% for some regions in Canada. Lin *et al.* [5] proposed a patch-based information reconstruction method to remove cloud by utilizing cloud-contaminated multitemporal images. However, it only integrates multitemporal reference images for cloud removal in one target image, but it has not taken mutual cloud removal for all cloud-contaminated multitemporal images into consideration. Moreover, the prior information between cloud-free and cloud-contaminated pixels can be further dug out, particularly for the spatial constraint between the central pixel and similar pixels. However, existing methods such as MNSPI and STMRF directly assembled the spatial or temporal information from similar pixels.

To address the aforementioned issues, this paper presents a novel spatially and temporally weighted regression (STWR) model to produce continuous cloud-free Landsat imagery. STWR makes full use of cloud-free pixels in the input time-series cloud-contaminated scenes and optimally integrates both spatial and temporal information to restore missing data in each target scene. The major contribution of this paper focuses on solving a more complex and practical issue: continuous cloud removal. To be specific, our model aims to transfer time-series cloud-contaminated Landsat scenes to corresponding cloud-free ones. Moreover, a complete procedure of removing Landsat clouds, including cloud/shadow detection, cloud/shadow labeling, and cloud removal, was provided. The implementation of cloud removal using STWR can be easily extended to the reprocessing of cloud-free remote sensing productions.

The remainder of this paper is organized as follows: a detailed illustration of methodology is provided in Section II. Then, experimental tests with both simulated and actual data and algorithm comparisons are shown in Section III. Conclusions and some discussions regarding the implications of our approach are marked in Section IV.

II. METHODOLOGY

Fig. 1 presents the flowchart of the proposed STWR method for cloud removal. Cloud/shadow detection was primarily performed for all input cloud-contaminated Landsat scenes. Then, an automatic cloud numbering method was employed to label each separate cloud. Generally, the proposed STWR method recovers clouds patch by patch, and for each cloud patch, it recovers contaminated value pixel by pixel. The implementation of cloud removal included five substeps: 1) spatiotemporal selection of invariant similar pixels; 2) sorting the reference image patches; 3) STWR for restoring cloud-contaminated areas; 4) inverse distance weighted (IDW) interpolator for dead pixels; and 5) iterative cloud removal for the succeeding cloud-contaminated image.

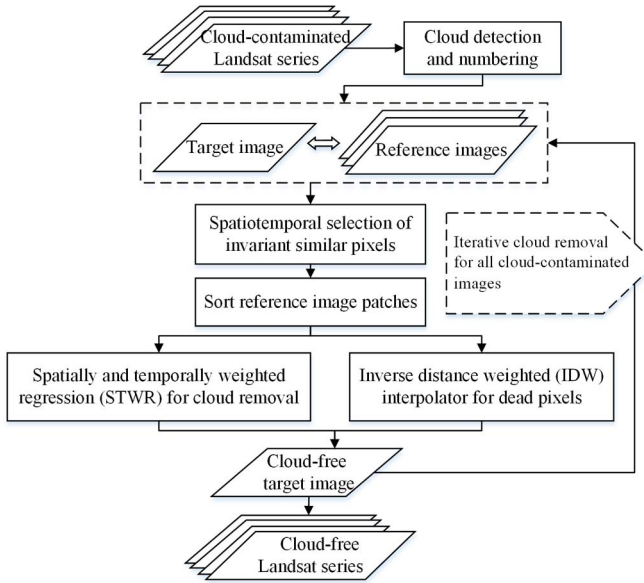


Fig. 1. Flowchart of the proposed STWR method.

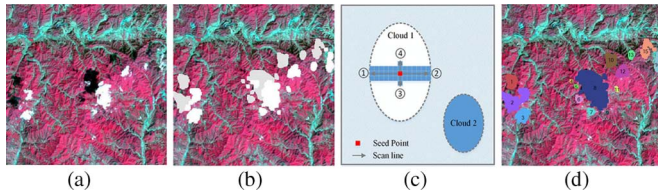


Fig. 2. Cloud detection and automatic numbering. (a) Original cloud-contaminated scene. (b) Cloud/shadow detection result using Fmask. The white area represents clouds, whereas the light gray area represents cloud shadow. (c) Schematic of automatic cloud numbering method. (d) Final labeled result of separate clouds.

A. Using Multiple Cloud-Contaminated Landsat Images as Input Data

1) *Cloud/Shadow Detection and Numbering*: Identification of clouds and cloud shadows is the primary step before the algorithm implementation. In this paper, an object-based detection method named Fmask [22] was employed, which has been applied in the cloud and cloud shadow detection of the USGS Landsat Surface Reflectance Climate Data Record (Landsat CDR) datasets (i.e., L4–5 TM, L7 ETM+, and L8 OLI/TIRS). For convenience in discussion, hereafter, we will simply group cloud and cloud shadows into cloud type. Once the cloud pixels are identified, we have to refine the cloud image into separate clouds because the subsequent cloud removal is designed to be processed patch by patch. For simplicity, we proposed an automatic cloud numbering method using a fast flood filling (i.e., scan-line filling) algorithm, to label each separate cloud and figure out the total number of cloud patches. Fig. 2 presents the practical implementation of cloud detection and automatic numbering, which includes two major steps: cloud/shadow detection using Fmask [see Fig. 2(b)] and automatic cloud numbering [see Fig. 2(c)]. The final labeled result of separate clouds is shown in Fig. 2(d).

2) STWR for Cloud Removal:

a) *Step 1—Spatiotemporal selection of invariant similar pixels*: Pixels having similar spectral and land-cover information are called similar pixels. Commonly, there are two

ways to search for spectral similar pixels: 1) an unsupervised classification is first applied to the reference image, and then those candidate neighbor pixels sharing the same cluster with the target pixel are assigned as similar pixels; and 2) a semi-empirical threshold is used to identify similar pixels based on the reflectance difference between the candidate neighbor pixels and the target pixel. It is generally assumed that similar pixels are spatially and temporally stable. In other words, the relative spatial locations of similar pixels will be coincident within multitemporal scene, and similar pixels will have similar temporal changing patterns. However, there are two potential situations regarding the spatiotemporal variation of similar pixels. First, different land-cover types share similar spectral information. For example, the vegetation may show close spectral characteristics to the soil background before becoming green. Second, the temporal change of similar pixels may have some spatial variability even for the same land-cover type. For example, vegetation with the same type shows different spectral variations due to different solar illumination or fertilizing conditions. The intersection of transient similar pixels from multitemporal scenes will help to obtain a more accurate and stable set of similar pixels. However, the threshold determination and pixels intersection requires a large computation cost.

By incorporating the former potential situations, we proposed a spatiotemporal selection strategy for invariant similar pixels. Here, we nominate the similar pixels that have consistent or similar temporal changing trends as invariant similar pixels. In addition to the requirement of spatial adjacency and spectral similarity within a scene, the temporal changing trend along with the input time-series scenes is also added to derive high-quality invariant similar pixels.

First, a simple least-squares linear regression is applied to capture the temporal trend for each candidate invariant similar pixel, i.e.,

$$t_b = a_b + k_b \cdot T + \varepsilon \quad (1)$$

where t_b represents the intensity value or surface reflectance in the b th band, T is the temporal date, a_b and k_b are fitted variables for the b th band (a_b is the intercept, and k_b is the temporal trend), and ε is the residual bias.

Cloud-free pixels with the corresponding position of all reference images will be included for use, and cloud-contaminated pixels will be excluded. However, we have two types of special situations. First, if only two scenes of the corresponding pixels are cloud free, the direct linear function will be employed, i.e.,

$$t_{2b} = a_b + k_b \cdot t_{1b} \quad (2)$$

where t_{1b} and t_{2b} represent the intensity value or surface reflectance of the b th band for the two corresponding cloud-free pixels. Second, if only one scene of the corresponding pixel is cloud free, the step of tracking temporal trend will be omitted.

The temporal trend will be regarded as a temporal feature to be combined with spectral features (Landsat bands green, red, and NIR in this paper) in the following unsupervised classification procedure within a local patch-based window. For robustness and efficiency, the k -means classifier will be used in

an unsupervised classification. Results show that the proposed strategy highly improves the quality of similar pixels while reducing the computation cost.

According to the first law of geography, pixels that are spatially adjacent are more similar than those that are spatially non-adjacent. However, nonlocal similarities are commonly found within a remotely sensed image because of the repeated ground information for a continuous terrestrial surface. Thus, the local similar pixels will be preferentially selected in this paper, and the nonlocal similarity within a larger patch-based window will also be taken into consideration when local similar pixels are not sufficient to meet the algorithm's requirement. In this paper, the lower limit of invariant similar pixel's number is 15, and if the number is more, we designate the upper limit as 30, i.e., if the number of similar pixels is over 30, we will only select the first 30 pixels having the highest similarity. Otherwise, the window size will expand until the lower limit of invariant similar pixels can be satisfied.

b) Step 2—Sort reference image patches: For each cloud-contaminated patch of the target scene, there will be potential cloud-free patches in the coincident position from the other reference scenes. Given the following two assumptions, i.e., the reference image having higher spectral similarity to the target image will provide more reliable information for the cloud-contaminated prediction of the target scene, and between the target and reference scenes, the spectral similarity of the local patch is not always consistent with that of the whole image, we sorted reference scenes by patch similarity instead of the whole image similarity. Thus, the priority of reference scenes will vary from one cloud-contaminated patch to another, and the local spatial and spectral variation will be fully taken into consideration.

The synthetic root mean square error (SRMSE) is defined as the measure to sort the patch priority as follows:

$$\text{SRMSE}_i = \sqrt{\frac{\sum_{b=1}^N \sum_{j=1}^M (R_{j,b}^i - T_{j,b})^2}{M \cdot N}}, \quad i = 1, 2, \dots, P \quad (3)$$

where M denotes the total number of cloud-free pixels within the rectangular box that completely covers the cloud-contaminated patch. It should be noted that the size of the rectangular box varies with the size and shape of different clouds, and the column and row of the rectangular box are extended with a plus factor of 2 based on the maximum boundary of the rectangular box of each cloud. N and P denote the total band and reference patch numbers. $T_{j,b}$ denotes the surface reflectance or intensity value of the j th pixel with the b th band in the target patch, and $R_{j,b}^i$ is that of the corresponding i th reference patch. Note that the pixels utilized to compute SRMSE are all cloud-free pixels that are situated around the cloud-contaminated patch. Before the calculation of SRMSE, a cloud-contaminated proportion (CCP) for each reference patches will be primarily computed to exclude those heavily cloud-contaminated reference patches. In this paper, the CCP upper threshold is set to be 70%; if the CCP of the reference scene is over 70%, it will not be chosen as one candidate reference.

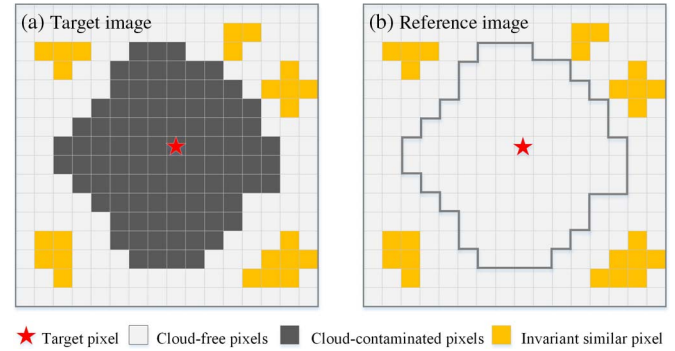


Fig. 3. Schematic of invariant similar pixels in both the target and reference images.

c) Step 3—Spatially weighted regression for the cloud-contaminated pixel's reconstruction: Once the set of invariant similar pixels and the priority of the reference patch were identified, we introduced the STWR model to reconstruct the missing value of a target scene from both a self-target scene and reference scenes. In this paper, the information of similar pixels on both the target image and reference image were used to reconstruct the missing value of the target pixel simultaneously. To be specific, the recovery prediction derived from the reference image is named first-term prediction, whereas the recovery prediction derived from the self-target image is named second-term prediction.

In the first term, we applied a spatially weighted regression method [23]–[25] to recover cloud-contaminated pixels of the target image. The main advantage that spatially weighted least squares enjoy over other methods is the ability to handle regression situations in which the similar pixels are of varying quality. As the set of invariant similar pixels has been defined, and for example in Fig. 3, a linear regression between the similar pixels on reference and target images can be easily depicted as

$$t(x_j, y_j, b) = \alpha_b \cdot r(x_j, y_j, b) + \beta_b \quad (4)$$

$$J(\alpha_b, \beta_b) = \frac{1}{M} \sum_{j=1}^M [t(x_j, y_j, b) - \alpha_b \cdot r(x_j, y_j, b) - \beta_b]^2 \quad (5)$$

where $t(x_j, y_j, b)$ and $r(x_j, y_j, b)$ denote the j th similar pixel on the target image and the reference image, respectively, and α_b and β_b are the regression coefficients, which can be solved by minimizing the cost function (5).

Then, the missing value of the target image can be recovered by multiplying a corresponding target pixel of the reference image with regression coefficients α_b and β_b . However, although the invariant similar pixels are filtered to be similar to the target pixel, their contribution to predict the target pixel's value might vary from the mutual similarity. For this reason, we introduced spatial weights to modify the cost function (5) as

$$J'(\alpha_b, \beta_b) = \frac{1}{M} \sum_{j=1}^M w_j \cdot [t(x_j, y_j, b) - \alpha_b \cdot r(x_j, y_j, b) - \beta_b]^2. \quad (6)$$

It is assumed that an invariant similar pixel being more spatially adjacent and spectrally comparable to the target pixel should be assigned with a larger weight in this paper. Thus, the weight quantifies the contribution of j th similar pixel, which is determined by the spatial distance and spectral similarity between a similar pixel and the target pixel, i.e.,

$$D_j = \sqrt{(x_j - x)^2 + (y_j - y)^2} \quad (7)$$

$$S_j = \sqrt{\frac{\sum_{b=1}^N (r(x_j, y_j, b) - r(x, y, b))^2}{N}} \quad (8)$$

where D_j and S_j denote the spatial distance weight and spectral similarity weight, respectively. D_j is calculated by the Euclidean distance between the target pixel (x, y) and candidate pixel (x_j, y_j) . S_j is computed through the spectral difference between the target pixel and the candidate pixel in all N bands.

Both these two weights are further normalized to make them comparable through

$$D_j = \frac{D_j - \min(D_j)}{\max(D_j) - \min(D_j)} + \varepsilon \quad (9)$$

$$S_j = \frac{S_j - \min(S_j)}{\max(S_j) - \min(S_j)} + \varepsilon \quad (10)$$

where $\max(\cdot)$ and $\min(\cdot)$ denote the maximization and minimization operators, respectively. ε is an adjusted constant, which is determined to be 1 in this paper, i.e.,

$$w_j = \frac{\frac{1}{(D_j \cdot S_j)}}{\sum_{j=1}^M \frac{1}{(D_j \cdot S_j)}}. \quad (11)$$

By differentiating $J'(\alpha_b, \beta_b)$ with respect to α_b and β_b and by letting the partial derivatives be zero, we have

$$\begin{aligned} \frac{\partial}{\partial \alpha_b} J'(\alpha_b, \beta_b) &= \frac{2}{M} \sum_{j=1}^M w_j \cdot r(x_j, y_j, b) \\ &\cdot [t(x_j, y_j, b) - \alpha_b \cdot r(x_j, y_j, b) - \beta_b] = 0 \end{aligned} \quad (12)$$

$$\begin{aligned} \frac{\partial}{\partial \beta_b} J'(\alpha_b, \beta_b) &= \frac{2}{M} \sum_{j=1}^M w_j \\ &\cdot [t(x_j, y_j, b) - \alpha_b \cdot r(x_j, y_j, b) - \beta_b] = 0. \end{aligned} \quad (13)$$

By abbreviating (12), (13), we can obtain

$$\alpha_b = \frac{\sum_{j=1}^M w_j \cdot [t(x_j, y_j, b) - \overline{t(x_j, y_j, b)}] \cdot [r(x_j, y_j, b) - \overline{r(x_j, y_j, b)}]}{\sum_{j=1}^M w_j \cdot [r(x_j, y_j, b) - \overline{r(x_j, y_j, b)}]^2} \quad (14)$$

$$\beta_b = \overline{t(x_j, y_j, b)} - \alpha_b \cdot \overline{r(x_j, y_j, b)} \quad (15)$$

where $\overline{t(x_j, y_j, b)}$ and $\overline{r(x_j, y_j, b)}$ are the mean values of all invariant similar pixels in the searching window on the target image and the reference image, respectively.

By substituting (4) with (14) and (15), we can easily compute the recovery prediction $t(x, y, b)$ through (4) in the first term. Hereafter, the first-term recovery prediction is denoted by $t_1(x, y, b)$ for better comprehension in convenience.

For the second term, instead of directly utilizing the invariant similar pixels to produce the second-term recovery prediction, we consider the prior knowledge from the reference image by adding a modification term as

$$\begin{aligned} t_2(x, y, b) &= \sum_{j=1}^M w_j \cdot t(x_j, y_j, b) + \lambda \\ &\cdot \left[r(x, y, b) - \sum_{j=1}^M w_j \cdot r(x_j, y_j, b) \right] \end{aligned} \quad (16)$$

where $t_2(x, y, b)$ denotes the second-term recovery prediction. The difference between the self-weighted prediction and true observation in the reference image can be utilized as a prior test to quantify the restoration biases. λ is an adjusted parameter, which is assigned to be the regression coefficient α_b in this paper.

Thus, a more accurate prediction can be obtained by a weighted combination of these two predicted terms through

$$T(x, y, b) = \frac{w_t}{w_s + w_t} \cdot t_1(x, y, b) + \frac{w_s}{w_s + w_t} \cdot t_2(x, y, b) \quad (17)$$

$$w_s = \frac{1}{\sqrt{\sum_{b=1}^N \sum_{j=1}^M (r(x_j, y_j, b) - \overline{r(x, y, b)})^2 / M \cdot N}} \quad (18)$$

$$w_t = \frac{1}{\sqrt{\sum_{b=1}^N \sum_{j=1}^M (t(x_j, y_j, b) - \overline{t(x, y, b)})^2 / M \cdot N}} \quad (19)$$

where w_s and w_t are spatial and temporal weights, which are determined by the landscape heterogeneity and temporal change extent, respectively [19], [26].

d) Step 4—Temporally weighted combination of transient reconstruction: Each reference patch can be utilized to recover the missing value of a target image, and its result is named as transient prediction in this paper. In order to reduce the computation expense, the most similar three patches of reference images will be chosen to recover the missing value according to the sorting sequence of the SRMSE computed in Step 2. Note that if the number of reference images is less than three, all the reference patches will be utilized. Moreover, the SRMSE between each reference patch and the target patch is employed as the weight q_i to combine all these transient predictions through

$$q_i = \frac{1/\text{SRMSE}_i}{\sum_{i=1}^P 1/\text{SRMSE}_i} \quad (20)$$

$$\hat{T}(x, y, b) = \sum_{i=1}^P q_i \cdot T_i(x, y, b) \quad (21)$$

where P indicates the number of reference patches; it is set as three when the number of candidate reference patches is not less than three. $T_i(x, y, b)$ is the transient prediction derived from the i th candidate reference image, and $\hat{T}(x, y, b)$ is the final prediction result of the target cloud-contaminated pixel.

e) Step 5—Tackling With Special Cases: A list of cloud-contaminated images are participated in our implementation; however, the cloud patches cannot be completely overlapped by the reference images, resulting in not all the available images being sufficient to recover the missing pixels. Thus, we have to tackle with the special case that some partial pixels are always cloud-contaminated in all available images, i.e., no cloud-free reference is available for some target pixels. For convenience, we call these pixels “dead pixels.” In this paper, we employed the IDW method within a 5×5 window to interpolate dead pixels, i.e.,

$$\hat{t}(x, y, b) = \sum_{j=1}^M \frac{1}{d^\phi} \cdot t(x_j, y_j, b) \quad (22)$$

where $\hat{t}(x, y, b)$ is the dead pixel, $t(x_j, y_j, b)$ is the cloud-free pixel that is spatially adjacent, d is the distance between the adjacent cloud-free pixel and dead pixel, and ϕ is a distance coefficient, which is set to be 2 in this paper.

The interpolator window is buffered by the covering areas of deal pixels with a constant size.

f) Step 6—Iterative cloud removal for all the cloud-contaminated images: When all cloud patches of the first target image are well recovered, the next cloud-contaminated image from the set of reference images will be regarded as the target image for a new round of cloud removal. Meanwhile, the original target image will be grouped into the set of reference images. The iterative cloud removal procedure will not be terminated until all cloud-contaminated images are recovered.

B. Using One Cloud-Free Landsat Image as Input

Existing cloud removal methods based on multitemporal complementation mainly focus on using one auxiliary cloud-free Landsat image as the input reference. In this paper, the cloud-free image cannot only be added into the set of reference images but also can serve as the single reference to recover all the missing pixels. The former issue can be instructed by the aforementioned Steps 3 and 4, and the latter issue will be only tackled with spatially weighted regression in Step 3.

III. RESULTS

A. Experimental Tests

To test the performance of our proposed method, experiments with both simulated and actual Landsat data were tested. For the simulated experiment, three Landsat-8 OLI scenes with band 3 (green), band 4 (red), and band 5 (NIR) acquired on September 1, October 3, and November 17, 2013, were contaminated by simulated clouds, respectively (see Fig. 4, Panel A). All the simulated clouds are randomly distributed in each Landsat image with varied shapes and areas. Panel B in Fig. 4 shows the

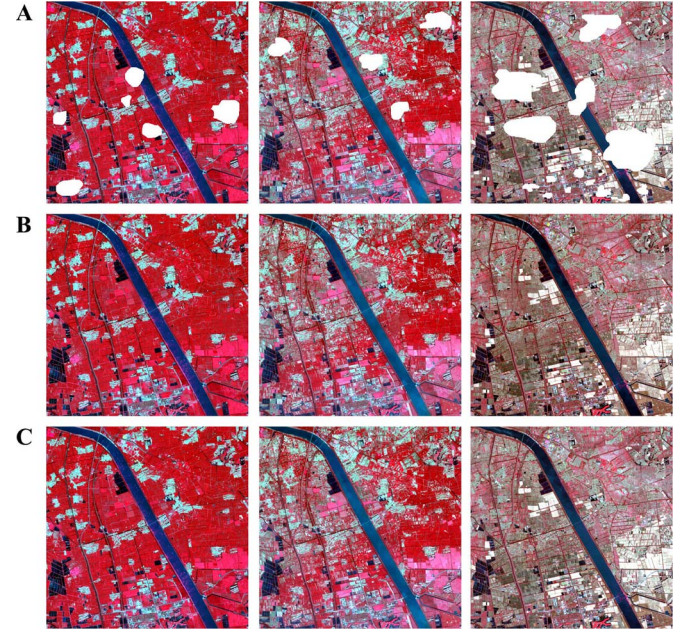


Fig. 4. Results of cloud removal for the simulated experiment. Panel A lists the NIR-red-green composites of Landsat-8 OLI images acquired on September 1, October 3, and November 17, 2013, which are contaminated by simulated clouds. Panel B lists the corresponding results of cloud removal using STWR method. Panel C lists the actual cloud-free images.

TABLE I
ACCURACY ASSESSMENT OF THE RECOVERY RESULT
IN THE SIMULATED EXPERIMENT

September 1			
Band	Green	Red	NIR
AAD	0.0062	0.0062	0.0062
RMSE	0.0096	0.0096	0.0096
October 3			
Band	Green	Red	NIR
AAD	0.0081	0.0081	0.0081
RMSE	0.0111	0.0111	0.0111
November 17			
Band	Green	Red	NIR
AAD	0.0096	0.0096	0.0096
RMSE	0.0286	0.0286	0.0286

recovery results of cloud removal for each cloud-contaminated image (see Fig. 4, Panel A). With a comparison with the actual cloud-free images (see Fig. 4, Panel C), our proposed STWR method produces robust and plausible visual results. The recovery results are shown to be quite similar to the actual ones in both spatial details and spectral comparability. The two quantitative measures (average absolute difference (ADD) and RMSE) in Table I also verify the possibility and efficiency of the proposed STWR method in producing continuous cloud-free images.

For the real experiment, four Landsat-5 TM images with band 2 (green), band 3 (red), and band 4 (NIR) acquired on May 5, July 24, August 9, and September 26, 2004 (see Fig. 5, Panel A) were utilized to test the performance of restoring continuous cloud-free images. Since the random coverage of cloud-contaminated areas in each input images, there is no one special scene that can provide sufficient cloud-free information for substituting cloud-contaminated areas in other scenes. However, with the concept of mutual substitution, the probability

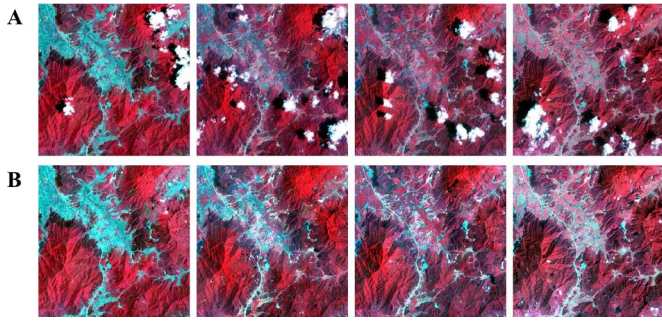


Fig. 5. Results of cloud removal for the actual Landsat-5 TM images. Panel A lists the actual cloud-contaminated images acquired on May 5, July 24, August 9, and September 26, 2004, respectively, and Panel B shows the corresponding results of cloud removal using the STWR method.

of continuous cloud-contaminated pixels in time-series Landsat scenes decreases significantly. Thus, we can make full use of all existing cloud-free information to better restore missing data caused by clouds or shadows. To be specific in Fig. 5, it is difficult to accurately restore cloud-contaminated areas with only the Landsat data acquired on May 5 and July 24 (or May 5 and August 9, or August 9 and September 26, and so on) because some cloud cover areas of these images completely overlap. In contrast, the number of such kinds of dead pixels will sharply decrease with four input continuous scenes, and the coverage of the remaining dead pixels is seldom large, which is appropriate for recovery by using some statistical methods such as IDW in this paper. The cloud removal results for each original cloud-contaminated image are shown in Panel C of Fig. 5. In addition, we have further tested another three study sites with different kinds of land-cover types using larger Landsat scenes (See in the appendix materials). The results show that STWR produces continuous cloud-free images in a high quality, which demonstrates the feasibility of our approach.

B. Algorithm Comparison

For the situation using one cloud-free Landsat image as input for cloud removal, three multitemporal-complementation-based methods including patch replacement (PR), the LLHM, the MNSPI, and the STMRF method were selected to compare with the proposed STWR method. Two groups of experiments with distinct landscape heterogeneity were conducted to qualitatively and quantitatively evaluate the efficacy of selected methods.

In the first experiment, a mountainous region in Landsat-8 OLI data with band 3 (green), band 4 (red), and band 5 (NIR) acquired on October 3, and November 4, 2013 was tested. The target scene [October 3, Fig. 6(a)] is primarily contaminated by three simulated thick clouds, and the reference scene [November 4, Fig. 6(b)] is used as the guide to recover cloud-contaminated information. The reconstruction results of four methods are shown in Fig. 6(c)–(g). Except for the PR method [see Fig. 6(c)] showing obvious visual biases due to the phenology change between the target and reference scenes, the other three methods all yield visually plausible results compared with the actual observation [see Fig. 6(h)]. Moreover, the

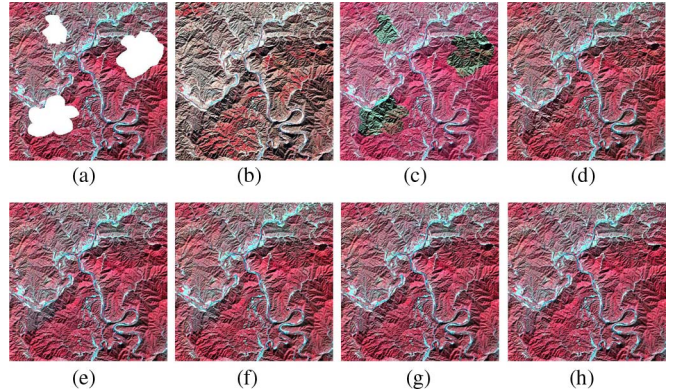


Fig. 6. Algorithm comparison in the first experimental site. (a) Simulated cloud-contaminated Landsat OLI image acquired on October 3, 2013. (b) Reference image acquired on November 4, 2014. (c)–(g) Results of cloud removal by PR, LLHM, MNSPI, STMRF, and the proposed STWR method, respectively. (h) Actual Landsat OLI image acquired on October 3, 2013.

TABLE II
ACCURACY ASSESSMENT OF RECOVERY RESULTS
IN THE FIRST EXPERIMENTAL SITE

	Bands	PR	LLHM	MNSPI	STMRF	STWR
AAD	Green	0.0092	0.0035	0.0033	0.0031	0.0029
	Red	0.0145	0.0062	0.0044	0.0042	0.0041
	NIR	0.0804	0.0207	0.0192	0.0178	0.0176
RMSE	Green	0.0111	0.0053	0.0050	0.0048	0.0046
	Red	0.0190	0.0090	0.0069	0.0069	0.0066
	NIR	0.0854	0.0271	0.0253	0.0239	0.0232
CC	Green	0.9337	0.9303	0.9269	0.9335	0.9379
	Red	0.8964	0.8933	0.9142	0.9173	0.9233
	NIR	0.8798	0.8828	0.8974	0.9098	0.9135
QI	Green	0.9737	0.9893	0.9888	0.9898	0.9904
	Red	0.9597	0.9820	0.9872	0.9875	0.9876
	NIR	0.9559	0.9836	0.9829	0.9853	0.9860
SSIM	Green	0.9767	0.9832	0.9932	0.9941	0.9939
	Red	0.9606	0.9752	0.9913	0.9915	0.9906
	NIR	0.9513	0.9712	0.9880	0.9901	0.9903

commonly used statistical indices including the AAD, RMSE, and correlation coefficient (CC) were chosen to quantitatively evaluate the recovery accuracy. Table II shows that our STWR method produces markedly lower biases than the other methods for all bands in terms of three different measures.

In the second experiment, a more heterogeneous region in true color Landsat-8 OLI data with band 2 (blue), band 3 (green), and band 4 (red) acquired on October 3, and November 4, 2013 were tested. Fig. 7(a) is the target image contaminated by five simulated clouds. Fig. 7(b) is the corresponding reference image. Visual inspection between Fig. 7(a) and (b) shows that both phenology and land-cover changes occur in this study site, which is a great challenge to restore missing information using only one prior reference image. With a visual inspection of all the recovery results in Fig. 7(c)–(g), for the PR method [see Fig. 7(c)], its recovery result shows a serious spectral distortion. For the LLHM method [see Fig. 7(d)], it keeps a consistent spectral comparability between the cloud-contaminated and cloud-free regions. However, its spatial details are not reliable, which shows a large bias compared with the actual observation [see Fig. 7(h)]. For the MNSPI method [see Fig. 7(e)], it shows a closer recovery result to the actual one, but its spatial details in the heterogeneous region are blurred to some extent. For the STMRF method [Fig. 7(f)], it

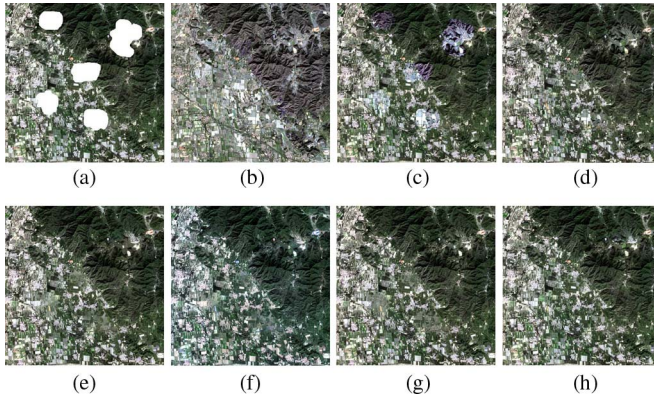


Fig. 7. Algorithm comparison in the second experimental site. (a) Simulated cloud-contaminated Landsat OLI image acquired on October 3, 2013. (b) Reference image acquired on November 4, 2014. (c)–(g) Results of cloud removal by PR, LLHM, MNSPI, STMRF, and the proposed STWR method, respectively. (h) Actual Landsat OLI image acquired on October 3, 2013.

TABLE III
ACCURACY ASSESSMENT OF RECOVERY RESULTS
IN THE SECOND EXPERIMENTAL SITE

	Bands	PR	LLHM	MNSPI	STMRF	STWR
AAD	Blue	0.0368	0.0177	0.0126	0.0126	0.0117
	Green	0.0179	0.0105	0.0081	0.0078	0.0074
	Red	0.0136	0.0081	0.0063	0.0058	0.0057
RMSE	Blue	0.0501	0.0269	0.0207	0.0211	0.0189
	Green	0.0270	0.0161	0.0131	0.0127	0.0115
	Red	0.0195	0.0123	0.0102	0.0094	0.0089
CC	Blue	0.5295	0.5266	0.6823	0.6730	0.7318
	Green	0.6402	0.6346	0.7356	0.7484	0.7909
	Red	0.6393	0.6446	0.7302	0.7587	0.7788
QI	Blue	0.9383	0.9532	0.9576	0.9588	0.9623
	Green	0.9528	0.9622	0.9626	0.9640	0.9669
	Red	0.9514	0.9601	0.9611	0.9643	0.9664
SSIM	Blue	0.9346	0.9424	0.9663	0.9674	0.9706
	Green	0.9566	0.9632	0.9726	0.9744	0.9768
	Red	0.9546	0.9589	0.9719	0.9756	0.9764

also achieves a good recovery result, but it cannot well capture land-cover changes that occurred in the upper right corner. For the STWR method [Fig. 7(g)], it shows the most plausible recovery result. With the integration of information on both the target image and reference image through a STWR model, STWR can efficiently restore cloud-contaminated information.

The quantitative assessment in Table III also shows the relative robustness and superiority of the STWR over the other cloud removal methods. Furthermore, zoomed subregions in both study sites were shown in Fig. 8; it could be seen that the STWR restores much closer information to actual cloud-free observation than other methods in both spatial details and spectral characteristics. However, due to the land-cover change between the target and reference images, Fig. 8(e) cannot accurately restore consistent information to the original cloud-free image [see Fig. 8(f)], but it still produces the optimum recovery result.

IV. CONCLUSION AND DISCUSSION

This paper has developed a novel STWR model for cloud removal to produce continuous cloud-free Landsat images. The proposed method makes full utilization of cloud-free

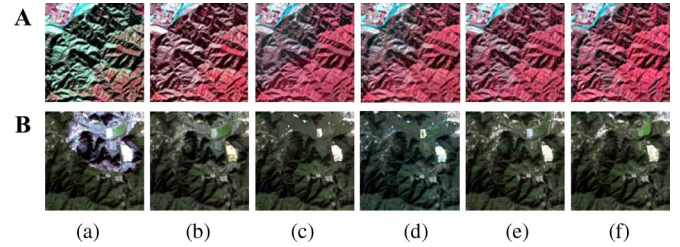


Fig. 8. Zoomed regions cropped from the recovery results in the first experimental site (Panel A) and the second experimental site (Panel B). (a)–(e) Zoomed results by PR, LLHM, MNSPI, STMRF, and the proposed STWR method, respectively. (e) is the actual zoomed image.

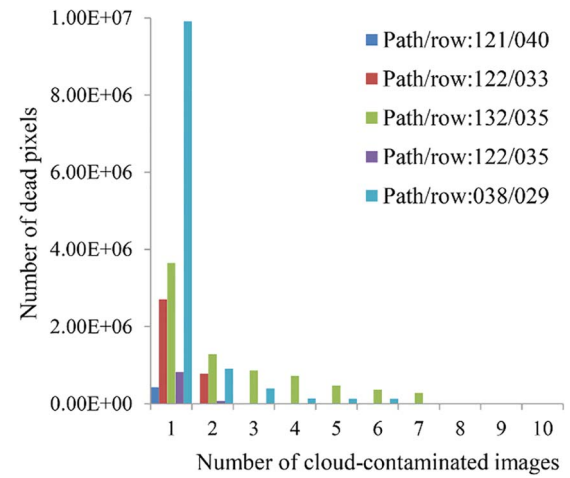


Fig. 9. Correlation bar between the number of dead pixels and cloud-contaminated images.

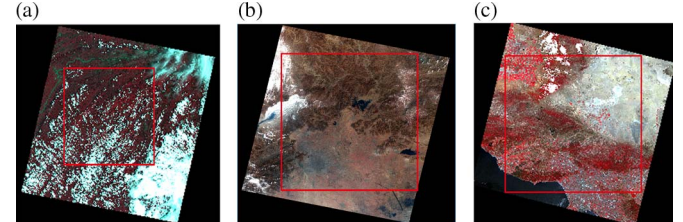


Fig. 10. Locations of three selected study sites for experimental tests. (a)–(c) First to third study sites with image sizes 3500 × 3500, 5000 × 5000, and 5000 × 5000, respectively.

information from input Landsat scenes and employs a STWR model to optimally integrate complementary information from invariant similar pixels. Moreover, a prior modification term is added to minimize biases derived from the spatially-weighted-regression-based prediction for each reference image. This approach provides a complete framework for continuous cloud removal and has the potential to be used for other optical images and applied to the reprocessing of cloud-free remote sensing productions.

The STWR model has been tested in both simulated and actual Landsat series data, and yields visually and quantitatively plausible recovery results. Compared with other cloud removal methods (PR, LLHM, and MNSPI), our method produces lower biases and more robust efficacy. The relatively robust and

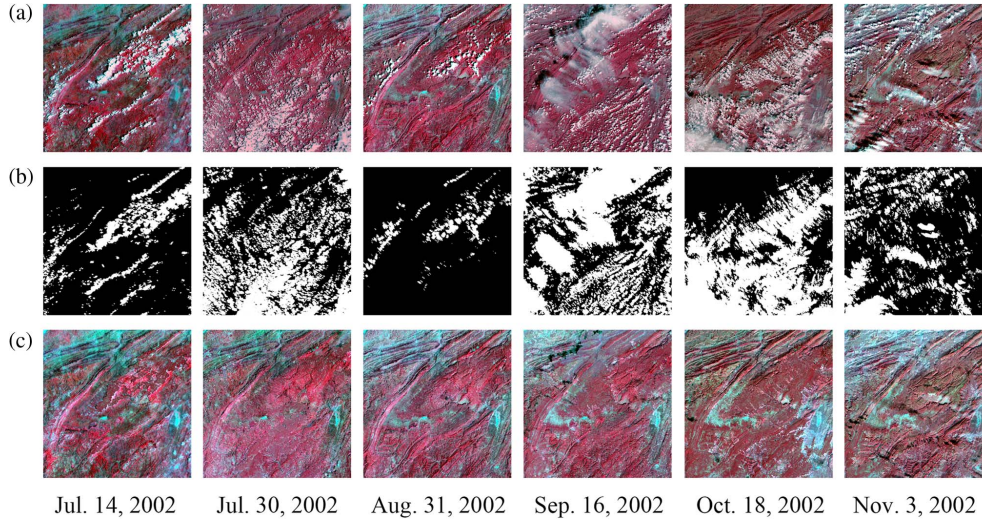


Fig. 11. Continuous cloud removal tests with large Landsat scenes (3500×3500) located in Enshi, Hubei, China (path: 126, row: 39). (a) Original cloud-contaminated scenes. (b) Corresponding cloud masks. (c) recovered cloud-free results.

accurate accuracy of our proposed method may be due to the following strengths.

First, multitemporal Landsat scenes provide more complementary information for restoring cloud-contaminated pixels. Recovering dead pixels that are continuously cloud contaminated is the most challenging part for cloud removal. However, with the increase in multitemporal Landsat scenes, the probability of remaining dead pixels will be cut down significantly. To study the statistical properties of the probability of dead pixels versus the input number of Landsat scenes, we download Landsat observations for five randomly selected sites (path/row: 121/40, 122/33, 132/35, 122/35, and 38/29), and ten continuous cloud-contaminated Landsat images are acquired for each site. In Fig. 9, we can find that the number of dead pixels decreases obviously with the increase in cloud-contaminated images for all five selected scenes. In particular, for scenes (path/row: 121/40, 122/33, and 122/35), the number of dead pixels is approximate to zero when the number of cloud-contaminated images reaches up to three. For another two scenes, dead pixels also disappear when the number of cloud-contaminated images is over seven.

On the other hand, by means of sorting the reference patches from multitemporal Landsat scenes, the optimal reference patches that are more like the target one will be picked out to reconstruct the missing information in the target scene. Finally, the temporal weighted combination of all transient predictions from each selected reference patch also reduces the stochastic errors caused by different illumination or atmospheric conditions.

Second, the spatiotemporal selection of invariant similar pixels improves the quality and accuracy of the similar set of pixels. It has been mentioned in Section II about the spatiotemporal variation of similar pixels. Thus, in our method, similar pixels having consistent or similar temporal changing trends are denoted invariant similar pixels. Given the multitemporal Landsat scenes, we could compute the temporal changing trend for cloud-free pixels. In addition to the requirement of spatial adjacency and spectral similarity within self-based scene, the

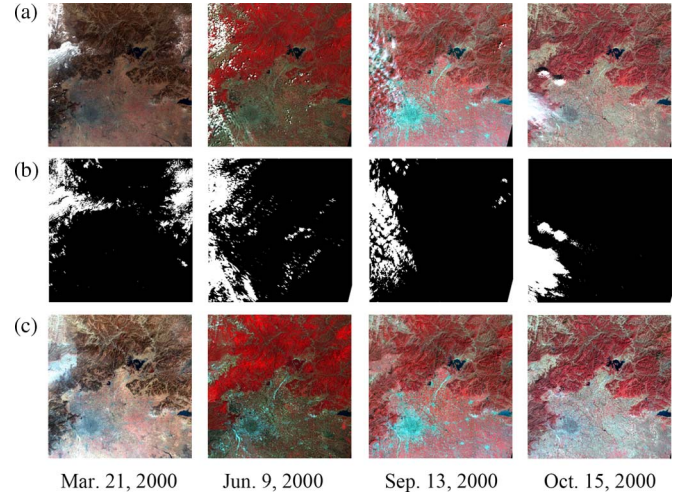


Fig. 12. Continuous cloud removal tests with large Landsat scenes (5000×5000) located in Beijing, China (path: 123, row: 32). (a) Original cloud-contaminated scenes. (b) Corresponding cloud masks. (c) recovered cloud-free results.

temporal changing trend along with the input time-series scenes is also added to derive high-quality invariant pixels.

Third, refining the spatially-weighted-regression prediction with a prior modification term can reduce the reconstruction biases. Previous studies such as filling ETM+ gaps using NSPI and weighted linear regression and removing clouds using MNSPI and STMRF integrate spatial and spectral information of similar pixels on target image through a weighted combination. However, there are fewer methods addressing its possible uncertainty derived from the reconstruction using spatially weighted regression or combination. Since the reference image is a good piece of prior knowledge for us to test and quantify the bias derived from the spatially weighted regression or combination. For these reasons, our method proposed to add a modification term into the simple spatially regression model.

Meanwhile, there are still some potential concerns regarding the implementation of STWR. First, all the tested time-series

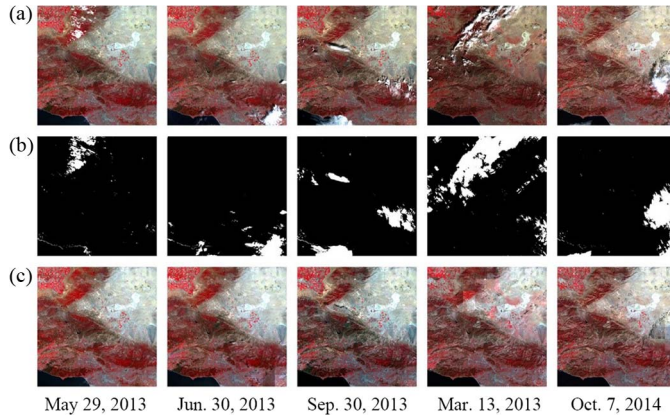


Fig. 13. Continuous cloud removal tests with large Landsat scenes (5000×5000) located in Los Angeles, CA, USA (path: 41, row: 36). (a) Original cloud-contaminated scenes. (b) Corresponding cloud masks. (c) recovered cloud-free results.

images are Landsat CDR Product, which has been radiometrically and atmospherically corrected. Thus, the mutual difference caused by solar illumination and atmospheric conditions are neglected in this paper. If the remote sensing data in level 1 is utilized, we suggest performing prior intensity normalization between target and reference images. For example, Lin *et al.* [5] normalized the intensity values of target and reference images using a linear transformation. Second, the proposed method is incapable of restoring accurate information when obvious land-cover change occurs. Third, it has been widely confirmed that there will always be much similar information within a single remotely sensed image. Moreover, such kind of similar information not only exists in spatially adjacent local similarity but also in nonlocal similarity. Thus, our method suggests performing a prior unsupervised classification of cloud-free pixels in reference images, which can be served as nonlocal backup candidates when local similar pixels are limited. Forth, dead pixels may still exist in time-series images. Without any prior information, an IDW interpolator can accurately recover the dead pixels when the landscape is relative homogeneous. However, it will produce some biases when the landscape is heterogeneous. Thus, some geostatistical methods such as kriging or co-kriging can be used to make full use of geospatial correlation. Moreover, some multisource image fusion methods are also recommended to be incorporated to solve this shortcoming.

APPENDIX MATERIALS

Here, the STWR's experimental tests in another three study sites with different land-cover types using larger Landsat scenes are studied. Spatial locations of selected study sites are shown in Fig. 10.

The first study site was located in Enshi, Hubei, China (path: 126, row: 39). This study area is dominated by continuous mountains and valleys, which is a heterogeneous site to test the algorithm's performance. Six Landsat-5 TM scenes acquired on July 14, July 31, August 31, September 16, October 18, and November 3, 2002 were utilized.

The second site was located in Beijing, China (path: 123, row: 32). It is characterized by open alluvial plains in the south

and east, and sheltering hills and mountains dominating the northern, northwestern, and western sides, and the elevations of the study site ranges from 10 m at the lowest location to 2303 m at the peak. The combination of heterogeneous urban and mountainous areas, and the ample land-cover types in the study area, comprising forest, impervious region, water, cropland, bare land, and grassland, provides us an ideal study region to test the algorithm's performance. Four Landsat-5 TM scenes acquired on March 21, June 9, September 13, and October 15, 2000, were utilized.

The third site was located in Los Angeles, CA, USA (path: 41, row: 36). This study area consists of various land covers, including water, developed urban, barren soil, forest, shrubs, and cultivated lands. The primary mountain ranges are Santa Monica Mountains and the San Gabriel Mountains in the southwestern and southeastern parts of Los Angeles County, respectively. Five Landsat-8 OLI scenes acquired on May 29, 2013, June 30, 2013, September 30, March 13, 2014, and October 7, 2014, were utilized.

All of the three experimental results are shown in Figs. 11–13, with the upper row denoting the original cloud-contaminated Landsat scenes, the middle row denoting the corresponding cloud/shadow mask, and the bottom row denoting the final cloud-free results using STWR's continuous cloud removal. Results [see Fig. 11(c), Fig. 12(c), and Fig. 13(c)] show that our proposed algorithm can produce plausible cloud-removal results as well, even in larger study sites with different land-cover types, as the number of acquired reference cloud-contaminated images depends on the proportion of dead pixels (pixels with same locations are continuously contaminated by cloud). Generally, the total number of dead pixels will decrease dramatically with the increase in multitemporal Landsat scenes (see Fig. 9), and this paper suggests that around five Landsat scenes is appropriate to implement continuous cloud removal for large scenes.

ACKNOWLEDGMENT

The authors would like to thank Prof. H. Shen and Dr. Q. Cheng from Wuhan University for the experimental tests using the STMRRM method, and the two anonymous reviewers and the external editor for providing valuable suggestion and comments, which have greatly improved this paper.

REFERENCES

- [1] D. Williams, S. Goward, and T. Arvidson, "Landsat: Yesterday, today, and tomorrow," *Photogramm. Eng. Remote Sens.*, vol. 72, no. 10, pp. 1171–1178, 2006.
- [2] M. A. Wulder, J. G. Masek, W. B. Cohen, T. R. Loveland, and C. E. Woodcock, "Opening the archive: How free data has enabled the science and monitoring promise of Landsat," *Remote Sens. Environ.*, vol. 122, pp. 2–10, Jul. 2012.
- [3] M. A. Wulder *et al.*, "Landsat continuity: Issues and opportunities for land cover monitoring," *Remote Sens. Environ.*, vol. 112, no. 3, pp. 955–969, Mar. 2008.
- [4] C. E. Woodcock *et al.*, "Free access to Landsat imagery," *Science*, vol. 320, no. 5879, pp. 1011–1011, May 2008.
- [5] C.-H. Lin, K.-H. Lai, Z.-B. Chen, and J.-Y. Chen, "Patch-based information reconstruction of cloud-contaminated multitemporal images," *IEEE Trans. Geosci. Remote Sens.*, vol. 52, no. 1, pp. 163–174, Jan. 2014.
- [6] D. P. Roy *et al.*, "Multi-temporal MODIS—Landsat data fusion for relative radiometric normalization, gap filling, and prediction of Landsat data," *Remote Sens. Environ.*, vol. 112, no. 6, pp. 3112–3130, 2008.

- [7] J. Ju and D. P. Roy, "The availability of cloud-free Landsat ETM+ data over the conterminous United States and globally," *Remote Sens. Environ.*, vol. 112, no. 3, pp. 1196–1211, Mar. 2008.
- [8] B. Chen, B. Huang, and B. Xu, "Comparison of spatiotemporal fusion models: A review," *Remote Sens.*, vol. 7, no. 2, pp. 1798–1835, 2015.
- [9] B. Chen, B. Huang, and B. Xu, "Fine land cover classification using daily synthetic Landsat-like images at 15-m resolution," *IEEE Geosci. Remote Sens. Lett.*, vol. 12, no. 12, pp. 2359–2363, Dec. 2015.
- [10] C.-H. Lin, P.-H. Tsai, K.-H. Lai, and J.-Y. Chen, "Cloud removal from multitemporal satellite images using information cloning," *IEEE Trans. Geosci. Remote Sens.*, vol. 51, no. 1, pp. 232–241, Jan. 2013.
- [11] P. Rakwatin, W. Takeuchi, and Y. Yasuoka, "Restoration of aqua MODIS band 6 using histogram matching and local least squares fitting," *IEEE Trans. Geosci. Remote Sens.*, vol. 47, no. 2, pp. 613–627, Feb. 2009.
- [12] Y. Zhang, B. Guindon, and J. Cihlar, "An image transform to characterize and compensate for spatial variations in thin cloud contamination of Landsat images," *Remote Sens. Environ.*, vol. 82, no. 2/3, pp. 173–187, 2002.
- [13] C. Y. Ji, "Haze reduction from the visible bands of LANDSAT TM and ETM+ images over a shallow water reef environment," *Remote Sens. Environ.*, vol. 112, no. 4, pp. 1773–1783, 2008.
- [14] N. T. Hoan and R. Tateishi, "Cloud removal of optical image using SAR data for ALOS applications: Experimenting on simulated ALOS data," *J. Remote Sens. Soc. Jpn.*, vol. 29, no. 2, pp. 410–417, 2009.
- [15] B. Huang, Y. Li, X. Han, Y. Cui, W. Li, and R. Li, "Cloud removal from optical satellite imagery with SAR imagery using sparse representation," *IEEE Geosci. Remote Sens. Lett.*, vol. 12, no. 5, pp. 1046–1050, May 2015.
- [16] F. Melgani, "Contextual reconstruction of cloud-contaminated multitemporal multispectral images," *IEEE Trans. Geosci. Remote Sens.*, vol. 44, no. 2, pp. 442–455, Feb. 2006.
- [17] S. Benabdelkader and F. Melgani, "Contextual spatiotemporal postreconstruction of cloud-contaminated images," *IEEE Geosci. Remote Sens. Lett.*, vol. 5, no. 2, pp. 204–208, Feb. 2008.
- [18] M. Li, S. C. Liew, and L. K. Kwoh, "Producing cloud free and cloud-shadow free mosaic from cloudy IKONOS images," in *Proc. IEEE IGARSS*, 2003, vol. 6, pp. 3946–3948.
- [19] X. Zhu, F. Gao, D. Liu, and J. Chen, "A modified neighborhood similar pixel interpolator approach for removing thick clouds in Landsat images," *IEEE Geosci. Remote Sens. Lett.*, vol. 9, no. 2, pp. 521–525, Feb. 2012.
- [20] Q. Cheng, H. Shen, L. Zhang, Q. Yuan, and C. Zeng, "Cloud removal for remotely sensed images by similar pixel replacement guided with a spatio-temporal MRF model," *ISPRS J. Photogramm. Remote Sens.*, vol. 92, pp. 54–68, 2014.
- [21] D. G. Leckie, "Advances in remote sensing technologies for forest surveys and management," *Can. J. Forest Res.*, vol. 20, no. 4, pp. 464–483, 1990.
- [22] Z. Zhu and C. E. Woodcock, "Object-based cloud and cloud shadow detection in Landsat imagery," *Remote Sens. Environ.*, vol. 118, pp. 83–94, 2012.
- [23] D. Ruppert and M. P. Wand, "Multivariate locally weighted least squares regression," *Ann. Statist.*, vol. 22, no. 33, pp. 1346–1370, 1994.
- [24] C. Zeng, H. Shen, and L. Zhang, "Recovering missing pixels for Landsat ETM + SLC-off imagery using multi-temporal regression analysis and a regularization method," *Remote Sens. Environ.*, vol. 131, pp. 182–194, 2013.
- [25] B. Huang, B. Wu, and M. Barry, "Geographically and temporally weighted regression for modeling spatio-temporal variation in house prices," *Int. J. Geograph. Inf. Sci.*, vol. 24, no. 3, pp. 383–401, 2010.
- [26] J. Chen, X. Zhu, J. E. Vogelmann, F. Gao, and S. Jin, "A simple and effective method for filling gaps in Landsat ETM+ SLC-off images," *Remote Sens. Environ.*, vol. 115, no. 4, pp. 1053–1064, Apr. 2011.



Bo Huang (A'12) received the Ph.D. degree in remote sensing and mapping from the Institute of Remote Sensing Applications, Chinese Academy of Sciences, Beijing, China, in 1997.

From 2001 to 2004, he was with the faculty of the Department of Civil Engineering, National University of Singapore, Singapore, and from 2004 to 2006, with the Schulich School of Engineering, University of Calgary, Calgary, AB, Canada. He is currently a Professor with the Department of Geography and Resource Management, The Chinese University of Hong Kong, Shatin, Hong Kong, where he is also the Associate Director of the Institute of Space and Earth Information Science. His research interests include most aspects of geoinformation science, specifically spatiotemporal image fusion for environmental monitoring, spatial/spatiotemporal statistics for land-cover/land-use change modeling, and multiobjective spatial optimization for sustainable land-use planning. He is currently exploring along the line of precision remote sensing, convinced that this new paradigm will revolutionize the way how multisensor remotely sensed data are fused and exploited to improve the performance and quality of various applications in the future.

Dr. Huang serves as the Executive Editor of *Annals of GIS* and the Asia-Pacific Editor of the *International Journal of Geographical Information Science*.



Lifan Chen received the B.S. degree in physics and the Ph.D. degree from Beijing Normal University, Beijing, China, in 2011 and 2016, respectively.

She is currently a Climatic Data Researcher with the National Meteorological Information Center, China Meteorological Administration, Beijing, China. Her research interests include remote sensing data fusion and dynamic modelling of wetland ecosystems.



Bing Xu received the M.S. and Ph.D. degrees in environmental science from the University of California, Berkeley, CA, USA, in 2001 and 2003, respectively.

From 2003 to 2004, she was an Assistant Professor of geography with the Texas State University, San Marcos, TX, USA, and from 2004 to 2008, with the University of Utah, Salt Lake City, UT, USA. She is currently a Professor with the Center for Earth System Science, Tsinghua University, Beijing, China. She is the author of six book chapters and

80 journal articles, including *PNAS*, *Annals of the AAG*, *Emerging Infectious Diseases*, *Remote Sensing of Environment*, *Nature Climate Change*, *ISPRS Journal of Photogrammetry and Remote Sensing*, *Environment International*, *Scientific Reports*, *PLoS NTD*, etc. Her research interests include multispatial, temporal, spectral resolution remotely sensed data fusion and change detection; pattern, process, and agent-based modeling of infectious disease transmission and pathogen evolution; and the biological aspects of pathogen, host, and their interactions.

Dr Xu served as the President of Chinese Professionals in Geographic Information Science from 2006 to 2007, and was on the board of directors from 2011 to 2013. She served as the Editor of the *Annals of Geographic Information Sciences* in 2009. She has received a number of research awards, including William A. Fischer Memorial Scholarship Award from the American Society for Photogrammetry and Remote Sensing, Early Career Award from Remote Sensing Specialty Group, Association of American Geographers, and Superior Research Award from the University of Utah.



Bin Chen (S'16) received the B.S. degree in geographical information systems from Wuhan University, Wuhan, China, in 2013. He is currently working toward the Ph.D. degree in global environmental change with the College of Global Change and Earth System Science, Beijing Normal University, Beijing, China.

His research interests include remote sensing image processing, multisource data fusion, and satellite-based environmental studies.